Magnetic aspect sensitivity of 3-m *F*-region field-aligned plasma density irregularities over Jicamarca

D. L. Hysell,[1] R. B. Hedden,[2,3] W. E. Swartz,[2] D. T. Farley,[2] J. L. Chau,[4] and M. A. Milla[4]

Received 18 May 2011; revised 1 July 2011; accepted 15 July 2011; published 1 October 2011.

[1] The magnetic aspect angle sensitivity of 3-m plasma density irregularities in the *F*-region ionosphere over Jicamarca has been measured during the passage of a radar plume in an equatorial spread-*F* event. The measurement technique utilizes radar interferometry with a number of antenna baselines with different lengths and orientations. Several corrections are applied to the data to reduce experimental biases. The RMS aspect angle half widths (the square root of the angular variance, the standard deviation) were found to be 0.01 ± 0.005° in a bottomside layer and near the top of the plume and 0.02 ± 0.005° in the central channel of the plume near *F*-peak altitudes. In the frequency domain, the magnetic aspect width was narrowest at small Doppler shifts and broader in the wings of the spectra when wings existed. These findings appear to be reasonably consistent with theoretical predictions, although questions remain.

Citation: Hysell, D. L., R. B. Hedden, W. E. Swartz, D. T. Farley, J. L. Chau, and M. A. Milla (2011), Magnetic aspect sensitivity of 3-m *F*-region field-aligned plasma density irregularities over Jicamarca, *J. Geophys. Res.*, *116*, A10302, doi:10.1029/2011JA016856.

1. Introduction

[2] Small-scale plasma density irregularities in the ionosphere are known to be highly elongated in the direction of the geomagnetic field, owing to the highly anisotropic plasma mobilities and conductivities. Coherent radar backscatter from the irregularities can consequently be detected only when the scattering wave vector is close to perpendicular to the magnetic field. This phenomenon is referred to as magnetic aspect sensitivity. Measuring magnetic aspect sensitivity can be challenging, since the range of angles through which backscatter is detected is generally much narrower than the beam width of radars used for upper atmospheric research, implying a potentially poorly conditioned deconvolution problem (see, for example, the pioneering auroral backscatter studies carried out by *Leadabrand et al.* [1965] and others summarized by *Oksman et al.* [1986]). Refraction and other effects can further complicate the problem. Attempting the measurements is important, however, since they offer unique, quantitative insights into small-scale irregularity formation and dissipation processes. The mechanism responsible for generating plasma density irregularities with scale sizes comparable to or less than the ion gyroradius is a fundamental, unresolved problem, and measurements at microscales such as those described here are important for addressing it (see reviews by *Huba and Ossakow* [1979, 1981a, 1981b]).

[3] *Kudeki and Farley* [1989] pioneered the use of radar interferometry for measuring aspect sensitivity with high accuracy and precision, building on the basic interferometry technique introduced at Jicamarca by *Farley et al.* [1981]. The brightness distribution, the distribution of backscatter intensity versus bearing in the sky, is the two-dimensional Fourier transform of the visibility, the spatial autocorrelation function of the signals received on the ground. The first three moments of the former can be estimated from a measurement of the latter using a single interferometry baseline. Working at Jicamarca and measuring the cross-spectra of signals received with antenna module pairs displaced long distances parallel to **B**, *Kudeki and Farley* [1989] were able to estimate the RMS aspect angle half widths of plasma density irregularities in the equatorial electrojet. The figures they estimated were of the order of a few tenths of a degree. More refined versions of their experiment were performed recently by *Lu et al.* [2008], who recovered comparable but more extensive results.

[4] *Farley and Hysell* [1996] attempted similar experiments looking at *F* region irregularities associated with equatorial spread *F*. (For a contemporary review of ESF, see *Woodman* [2009].) The plasma is even more anisotropic at *F*-region altitudes than in the *E* region, and the RMS aspect widths of the irregularities are consequently smaller. *Farley and Hysell* [1996] had to correct for a number of systemic biases in their experiments in order to even detect the finite magnetic aspect width of the irregularities. Using a specialized means of calibration, they estimated the RMS aspect widths of irregularities in bottomside spread-*F* layers to be of the order of a few hundredths of a degree. (Note that their

[1]Earth and Atmospheric Sciences, Cornell University, Ithaca, New York, USA.
[2]Electrical and Computer Engineering, Cornell University, Ithaca, New York, USA.
[3]Johns Hopkins University Applied Physics Laboratory, Laurel, Maryland, USA.
[4]Radio Observatorio de Jicamarca, Instituto Geofísico del Perú, Lima, Peru.

0148-0227/11/2011JA016856

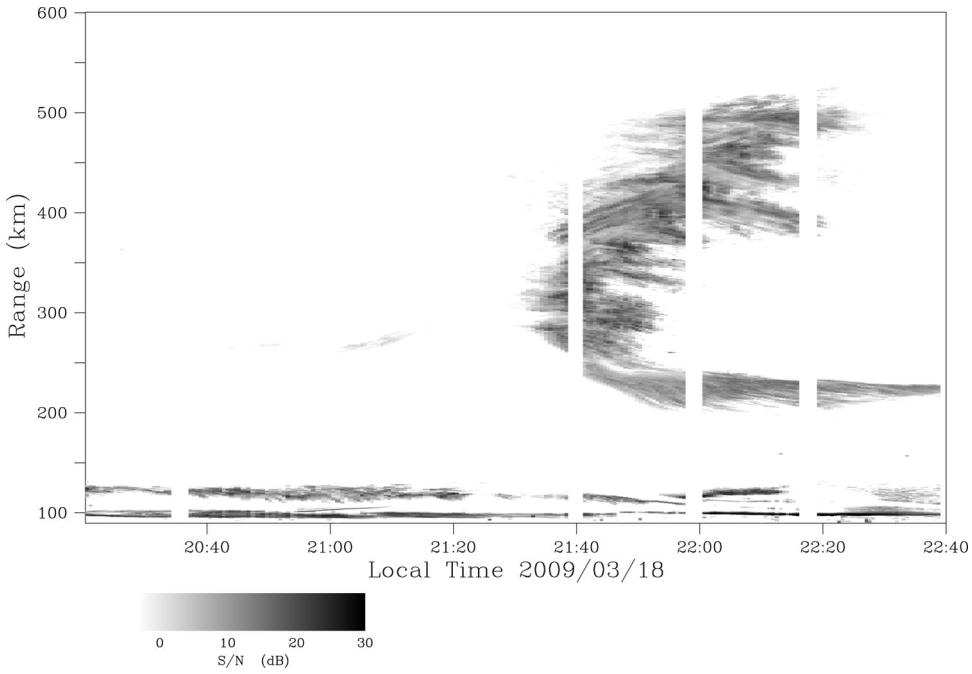

Figure 1. Range time intensity (RTI) representation of an ESF event observed on March 18, 2009, at the Jicamarca radio observatory. Gray scales indicate the signal-to-noise ratio on the scale indicated. A radar plume was visible between 2130–2230 LT, and a bottomside layer after 2140. Irregularities in the equatorial electrojet were present throughout. Data gaps represent intervals when samples were collected for internal consistency checks.

paper quoted estimates for the magnetic aspect angle RMS full width, whereas other studies, including the present one, discuss RMS half widths by convention. We will refer to the half width as the aspect width, the angular spread, or something similar here.) A theory to account for this result was outlined by *Hysell and Farley* [1996]. The magnetic aspect widths of irregularities within a spread-*F* plume were found to be somewhat greater than those in a bottomside layer, but the plume data were uncalibrated and therefore deemed to be less reliable.

[5] In this paper, we reexamine the magnetic aspect width of *F*-region plasma density irregularities. Improvements at Jicamarca have made the experiment more reliable, and many more interferometry baselines and altitudes can be sampled now. Below, we describe the experimental methodology and present the results of new measurements from a spread-*F* event which included both a bottomside layer and a radar plume. We discuss a number of data corrections still required for the experiment, assess the overall precision and accuracy of the results, and evaluate them in light of theory.

2. Experimental Methodology

[6] Experiments were conducted on March 17 and 18, 2009, at the Jicamarca Radio Observatory. Jicamarca is a modular, phased-array incoherent scatter radar located outside Lima, Peru, at 11°57′05″S latitude by 76°52′27.5″W longitude, where the magnetic dip angle is about 1°. Its main antenna is composed of 9216 crossed-dipoles tuned to 49.92 MHz. Jicamarca has three transmitters capable of transmitting 1.5 MW peak power each. A fourth transmitter is nearing completion. For the coherent scatter experiments described here, however, low-power driver stages were used for transmission. Digital receivers were used for reception.

[7] The experiments were made during solar minimum, when the effects of refraction, already small at the magnetic equator, were further minimized. The experiment utilized only the east and west quarters of the Jicamarca array for transmission, less module *b*, making the transmitter beam somewhat narrower in the east-west direction than it would be using the full array. Seven spaced antenna modules were used for reception (see below). The range resolution of the experiments was 300 m (2 μs pulses), and the interpulse period was 4 ms. Uncoded pulses were used. While spread-*F* irregularities were observed on both nights, we concentrate on data from the 18th, which alone exhibit a prototypical radar plume.

[8] The range-time-intensity (RTI) representation of the radar backscatter is shown in Figure 1. This event is typical of spread *F* in most respects except that the bottom-type layer, a common precursor of radar plumes, is barely noticeable here [*Hysell et al.*, 2004]. (Close examination shows the presence of a weak bottom-type layer at about 2105 LT, 270 km altitude.) Radar plumes are often visible over Jicamarca by 2000 LT. That this one arrived "late" may suggest that it was already past its main growth phase. That the Doppler shifts of the echoes (not shown) are relatively small supports this view. Horizontal streaks in the RTI plot indicate strong scattering regions passing from west to east through the radar beam. Irregularities occupying multiple layers are also visible in the equatorial electrojet throughout the event.

[9] The receiving antenna module arrangement for the experiments is diagrammed in Figure 2. Six independent modules within the main array were complemented by a

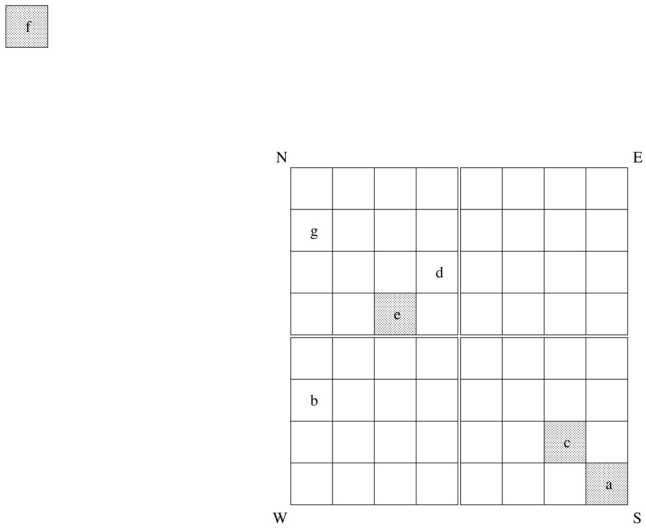

Figure 2. Plan view of the Jicamarca antenna array. Characters are the labels applied to different, independent receiving antenna modules. Shaded squares represent antenna modules used for this study. The module labeled "f" was deployed temporarily for long-baseline interferometry experiments. Note that the main antenna array main diagonal is directed 6.166° east of geographic north and that the magnetic declination at *F*-region altitudes over Jicamarca is taken to be 0.73° west of geographic north in March of 2009.

seventh, portable module situated several hundred meters to the north. The portable module was made from an array of Yagi antennas in such a way that its radiation pattern and gain were comparable to that of an antenna module. An attempt was made to situate the portable antenna so that baseline *af* would be precisely parallel to the magnetic field. However, the calculation was made using the available International Geomagnetic Reference Field (IGRF) model coefficients, which were out of date by 2009. New 2010 coefficients revealed that baseline *cf* turned out to be closer to parallel to the geomagnetic field at *F*-region altitudes in March of 2009.

[10] Details regarding the geometry of the receiving antenna modules are given in Table 1. For each antenna baseline of interest, the table gives the baseline length in meters, the clock angle the baseline made with the geomagnetic field in degrees, the horizontal projection of the baseline normal to **B**, the geomagnetic induction, in meters, and the ratio of this projection to the length of baseline *de*, which serves as a reference. As we discuss below, baselines with significant projections in the perpendicular-to-**B** direction represent sources of contamination, since the visibility is highly elongated in the direction of **B**. The table shows that the projection is smallest for baselines *ae* and *cf*. It is from these baselines that we mainly draw our conclusions.

[11] It is noteworthy that the geometry of the main Jicamarca antenna array as well as the portable antenna module were surveyed for this study using differential GPS. The orientation of the array main diagonal with respect to geographic north was found to be 6.166°, which differs slightly from the figure that appears in work by *Ochs* [1965], the standard reference at Jicamarca since construction. The *Ochs* [1965] figure, 6°1′, was stated without tolerances.

[12] The formalism for interpreting interferometry measurements at Jicamarca is given by *Hysell and Chau* [2006], whose work takes its conventions from *Thompson* [1986] but also covers error analysis and additional issues pertinent to applications in radar. The main points are summarized here. The normalized cross-correlation of the received signals from a pair of antennas separated in space by the vector baseline $\mathbf{d}_{ij}$, or the visibility function, i.e.

$$V(k;\mathbf{d}_{ij}) \equiv \frac{\left\langle v_i v_j^* \right\rangle}{\sqrt{\langle v_i^2 \rangle - N_i}\sqrt{\left\langle v_j^2 \right\rangle - N_j}}, \tag{1}$$

(where the angle brackets imply expectation and N_j refers to the system noise in the jth receiver channel) is related to the brightness distribution, the distribution of backscattered radiation intensity $B(k;\sigma)$, through the integral transform

$$V(k;\mathbf{d}_{ij}) = \int A_n(k;\sigma)B(k;\sigma)e^{ik\sigma\cdot\mathbf{d}_{ij}}d\Omega \tag{2}$$

where $A_n(k;\sigma)$ is the normalized antenna effective area, σ is a unit vector pointing someplace in the sky, the exponential term has the form of a point spread function, and $d\Omega$ is a solid angle interval. In the event that all the antennas are coplanar, then (2) can be written (with the i, j subscripts suppressed)

$$V(k;d_\perp,d_\parallel) = \int A_n(k;\eta,\xi)B(k;\eta,\xi)e^{ik\left(d_\perp\eta+d_\parallel\xi\right)}d\eta d\xi \tag{3}$$

where $d_\perp$ and $d_\parallel$ are the components of the baseline perpendicular and parallel to the projection of the geomagnetic field in the plane and where η and ξ are the direction cosines with respect to those directions. In writing (3), the geometry is assumed to be such that $\eta^2 + \xi^2 \ll 1$. In this limit, η and ψ can be interpreted as zenith angles in the planes perpendicular and parallel to **B**, respectively.

[13] The antenna effective area is dominated by the characteristics of the transmitting antenna array, which is large compared to the receive antennas. Combined, the antenna effective area and the brightness distribution limit the range of directions through which backscatter is received and serve as

Table 1. Geometry of Jicamarca Antenna Module Configuration[a]

Baseline	Length d (m)	Angle (deg)	$\lvert d_\perp \rvert$ (m)	$\lvert d_\perp \rvert$:$\overline{de}$
ac	50.912	6.895	6.112	0.120
ae	234.730	0.669	2.743	0.054
ag	336.134	2.552	14.967	0.294
af	641.507	0.776	8.683	0.171
ce	184.201	−1.048	3.370	0.066
cg	285.395	1.778	8.855	0.174
cf	590.911	0.249	2.571	0.051
eg	101.823	6.895	12.224	0.240
ef	406.778	0.837	5.940	0.117
fg	305.712	−1.178	6.284	0.123

[a]The columns are the antenna baseline, its length in meters, its clock angle with respect to the Earth's magnetic field in degrees, its length projected in the direction perpendicular to the magnetic field, and the ratio of that projection to the length of baseline *de*, respectively.

an effective brightness distribution, $B_{\text{eff}} = A_n B$. Accordingly, (3) can be expressed as a characteristic function:

$$V(k; d_\perp, d_\parallel) = \left\langle e^{ik(d_\perp \eta + d_\parallel \xi)} \right\rangle \tag{4}$$

where the angle brackets imply an average over the distribution B_{eff}, which serves as a normalized probability density function.

[14] The antenna effective area could easily determine how the modulus of the visibility, or the coherence, varies with $d_\perp$ but plays little role in the variation with $d_\parallel$ in practice, since the range of aspect angles from which backscatter is received is very small compared to the antenna beam width. Taking the brightness distribution to be a separable function of η and ξ, the coherence can be expressed as

$$\begin{aligned} |V(k; d_\perp, d_\parallel)| &= |V(k; d_\perp)||V(k; d_\parallel)| = \left|\left\langle e^{ikd_\perp \eta}\right\rangle\right|\left|\left\langle e^{ikd_\parallel \xi}\right\rangle\right| \\ &\approx \left(1 - \frac{k^2 d_\perp^2}{2}\left\langle (\eta - \langle\eta\rangle)^2 \right\rangle\right)\left(1 - \frac{k^2 d_\parallel^2}{2}\left\langle (\xi - \langle\xi\rangle)^2 \right\rangle\right) \\ &\approx e^{-\frac{1}{2}k^2 d_\perp^2 \delta\eta_{\text{rms}}^2} e^{-\frac{1}{2}k^2 d_\parallel^2 \delta\xi_{\text{rms}}^2} \end{aligned} \tag{5}$$

Here, $\delta\xi_{\text{rms}}$ is the desired (very small) RMS magnetic aspect angle, while the term involving $\delta\eta_{\text{rms}}$ is a bias term associated with potential baseline misalignment (making it important to keep $d_\perp^2$ as small as possible). Within the limits that (5) holds, surfaces of constant coherence are ellipses in planar baseline space, highly elongated in the direction parallel to **B**.

[15] Before presenting data, we point out a number of corrections that must be performed in order to estimate magnetic aspect width accurately. These arise from systemic and statistical aspects of the interferometry experiment.

2.1. Cable Length Corrections

[16] Special, impermanent cables are used to connect the antenna modules used for this experiment to the data acquisition equipment. The cables for the modules within the main array have effective lengths that differ by less than 50 m. In view of the 2 μs sampling time and the range overlap implied by the range-Doppler ambiguity functions for this experiment, the effect of those cable length differences is small although not entirely negligible. The cable that connects antenna module *f*, however, has an effective cable length that differs from the others by approximately 600 m, or about one sample interval. In practice, the samples coming from that module must be advanced in time (via phase advance in the Fourier domain) by just under 2 μs using an optimization procedure that maximizes the signal correlations. Similar albeit much smaller corrections must also be made for the other cables.

2.2. Bias Removal

[17] The most obvious estimator for (1) is

$$\hat{V}'(k; \mathbf{d}_{ij}) = \frac{\frac{1}{n}\sum_{l=1}^{n} v_{il} v_{jl}^*}{\sqrt{\frac{1}{n}\sum_{l=1}^{n}|v_{il}|^2 \frac{1}{n}\sum_{l=1}^{n}|v_{jl}|^2}} \tag{6}$$

where the n samples from the receivers, each labeled with a subscript l here, are taken to be statistically independent when error analysis is performed. As pointed out by *Farley* [1969], this estimator is biased. This is intuitively understandable; since the estimator cannot produce figures greater than unity, statistical errors will tend to cause underestimates, particularly when visibilities are close to unity. An unbiased estimator can be formed from the biased one using

$$\hat{V}(k; \mathbf{d}_{ij}) = \frac{\hat{V}'(k; \mathbf{d}_{ij})}{\sqrt{1 - \frac{1}{n}\left|\hat{V}'(k; \mathbf{d}_{ij})\right|^2}} \tag{7}$$

A more detailed description of estimator biases and corrections in interferometry can be found in work by *Hysell and Chau* [2006].

2.3. Error Analysis

[18] The key to this experiment lies in the fact that coherence estimates become extremely accurate in the high signal-to-noise ratio limit when the coherence is close to unity [*Farley*, 1969; *Farley and Hysell*, 1996]. If not for this fact, it would be quite impossible to measure RMS aspect angles of the order of one one-hundredth of a degree with the interferometry baselines available at Jicamarca. As shown by *Farley and Hysell* [1996], the mean squared error for the visibility estimate in this limit is

$$\delta^2 = \frac{1}{n}\left[\frac{N}{S} + \frac{1}{2}\epsilon + \mathcal{O}\left(\epsilon^2, \frac{N^2}{S^2}, \epsilon\frac{N}{S}, \cdots\right)\right] \tag{8}$$

where $\epsilon \equiv 1 - |V|^2$, n is the number of statistically independent samples used, and where S and N are the signal and noise powers, respectively. In our analysis, noise estimates are derived using a generalization of the method of *Hildebrand and Sekhon* [1974], which applies statistical tests to discriminate between signal and noise. From channel pairs, we calculate these from the geometric mean values. In view of (8) accurate measurements of a correlation of 0.995 could be achieved in the high signal-to-noise ratio limit using about 1000 samples or about 4 s. of integration time per Doppler spectral bin in this case.

2.4. Baseline Correction

[19] Small misalignments between the interferometry baseline and the geomagnetic field can reduce the coherence significantly, making magnetic aspect width measurements difficult. This is particularly true for shorter baselines in our experiments, for which the coherence in the absence of misalignment is expected to be very nearly unity. Equation (5) suggests a way to correct for misalignment bias using coherence measurements using a baseline with a predominantly zonal displacement ($d'_\perp$). Assuming that data exist for estimating $|V(k; d'_\perp)|$, one can develop a corrected magnetic aspect width estimator from

$$\left|V(k; d_\parallel)\right| \approx \frac{\left|V(k; d_\perp, d_\parallel)\right|}{|V(k; d'_\perp)|^{d_\perp^2/d_\perp'^2}} \tag{9}$$

[20] A problem with this strategy lies in the approximation

$$|V(k; d_\perp)| \approx e^{-\frac{1}{2}k^2 d_\perp^2 \delta\eta_{\text{rms}}^2} \tag{10}$$

which becomes increasingly poor as $d_\perp$ increases. Interferometry experiments with different baselines will tend to yield different estimates for $\delta\eta_{\text{rms}}$ if interpreted using (10), except

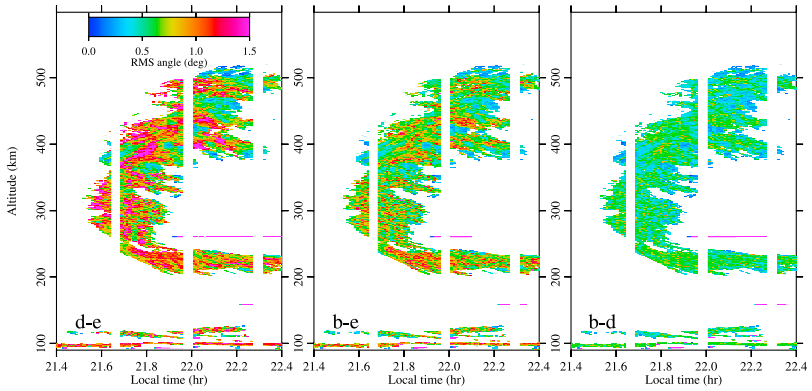

Figure 3. RMS half width of the scatterers in the zonal plane estimated using baselines *de* (the shortest), *be*, and *bd* (the longest), respectively. The scale is in degrees. If the Gaussian approximation of (10) were correct, all three panels should be essentially the same.

in the special case where the effective brightness distribution is Gaussian, in which case (10) holds exactly for all baseline lengths. Indeed, if this were not the case, there would be no utility in aperture synthesis imaging, which infers imagery of the brightness distribution from visibility data taken with multiple baselines [e.g., *Woodman*, 1997]. In fact, radar imagery of layers and plumes in ESF show them to be inhomogeneous and spatially intermittent rather than beam filling [*Hysell*, 2000].

[21] Figure 3 illustrates the point. Here are plotted estimates of $\delta\eta_{\rm rms}$ using data from three different, zonal antenna baselines. (Note that these are not magnetic aspect widths but instead widths in the plane perpendicular to **B**, measured in degrees.) The lengths of baselines *de*, *be*, and *bd* have the ratio 1:2:3. While some of the estimated widths are similar from frame to frame, the general trend is for the estimated width to decrease as the baseline used to measure it lengthens and the approximations leading to (10) break down.

[22] The perpendicular projections of the interferometry baselines available for aspect sensitivity measurements in Table 1 are all much smaller than the length of baseline *de*, the shortest purely zonal baseline available for correction. In practice, we find that the formula in (9) incorporating visibility measurements from *de* undercorrects for baseline misalignment errors. Artifacts following the general pattern of Figure 3, viz. areas of anomalously low correlation matching the red/violet regions in Figure 3, remain clearly visible in the RMS aspect width measurements even after correction. The effect is most severe where the baseline pointing error is greatest. A much better correction strategy involves using baseline *ac* for alignment error correction. Although this baseline is not purely zonal by any means, the displacement of the two antennas in the direction of the magnetic meridian is so small as to give rise to virtually no spatial decorrelation. We can therefore regard baseline *ac* as an estimator of $\delta\eta_{\rm rms}$ derived from a zonal interferometry baseline approximately 6 meters long.

[23] While baseline misalignment artifacts remain even after correcting the data using (9) with the coherence estimate from baseline *ac*, they appear to be modest in data obtained from baselines *ae* and *cf*, which have the smallest pointing error to begin with. The remainder of the analysis therefore concentrates on corrected data from those baselines. The fact that these two baselines have nearly the same misalignment suggest an alternative means of correction, as described below.

2.5. Diffraction and Other Geometric Factors

[24] Hardware imperfections aside, what, in principle at least, is the highest coherence value that could be measured? The curvature of the magnetic field might at first seem to be a limiting factor, but since the radius of curvature of the magnetic field lines is very large compared to that of the radar wavefronts in the *E* and *F* region, the magnetic field lines can actually be considered to be straight for all intents and purposes. For the moment, we will also take the magnetic field lines to be horizontal. The finite radius of curvature of the radar waves themselves poses an issue, however, since surfaces of constant altitude subtend tens of wavelengths measured radially from the radar within the solid angle illuminated by the Jicamarca antenna. This implies that coherent backscatter arises mainly from a Fresnel zone-sized region of the illuminated volume in the plane of the magnetic meridian. The horizontal extent L of the region at range R in that plane is given by $L = \sqrt{R\lambda/2}$, which is of the order of a kilometer in the *F* region. Does this finite spatial extent imply a minimum measurable value of the RMS parallel wave number of the ionospheric field-aligned irregularities responsible for the backscatter, independent of their intrinsic properties?

[25] As an idealized reference model of a perfectly field-aligned ionospheric irregularity, consider a single, horizontal wire of length L aligned with the magnetic meridian. The signal reflected by the wire will form a complicated diffraction pattern on the ground with a finite spatial correlation length. The reflected signal will not be resemble a single plane wave at ground level but will instead appear as a sum of plane waves with wave vectors with different amplitudes and wave vector direction cosines. This pattern could, in principle, be detected on the ground using appropriate spaced-antenna techniques. Since the different plane wave components have amplitudes that are perfectly correlated, however, the pattern will not be visible to the normalized correlation function (1) or its estimator (6). The measured coherence will be unity, regardless of the diffraction pattern on the ground, since the pattern affects the cross product and the normalization terms in (1) identically. Measured coherence values less than unity arise from distributions of plane

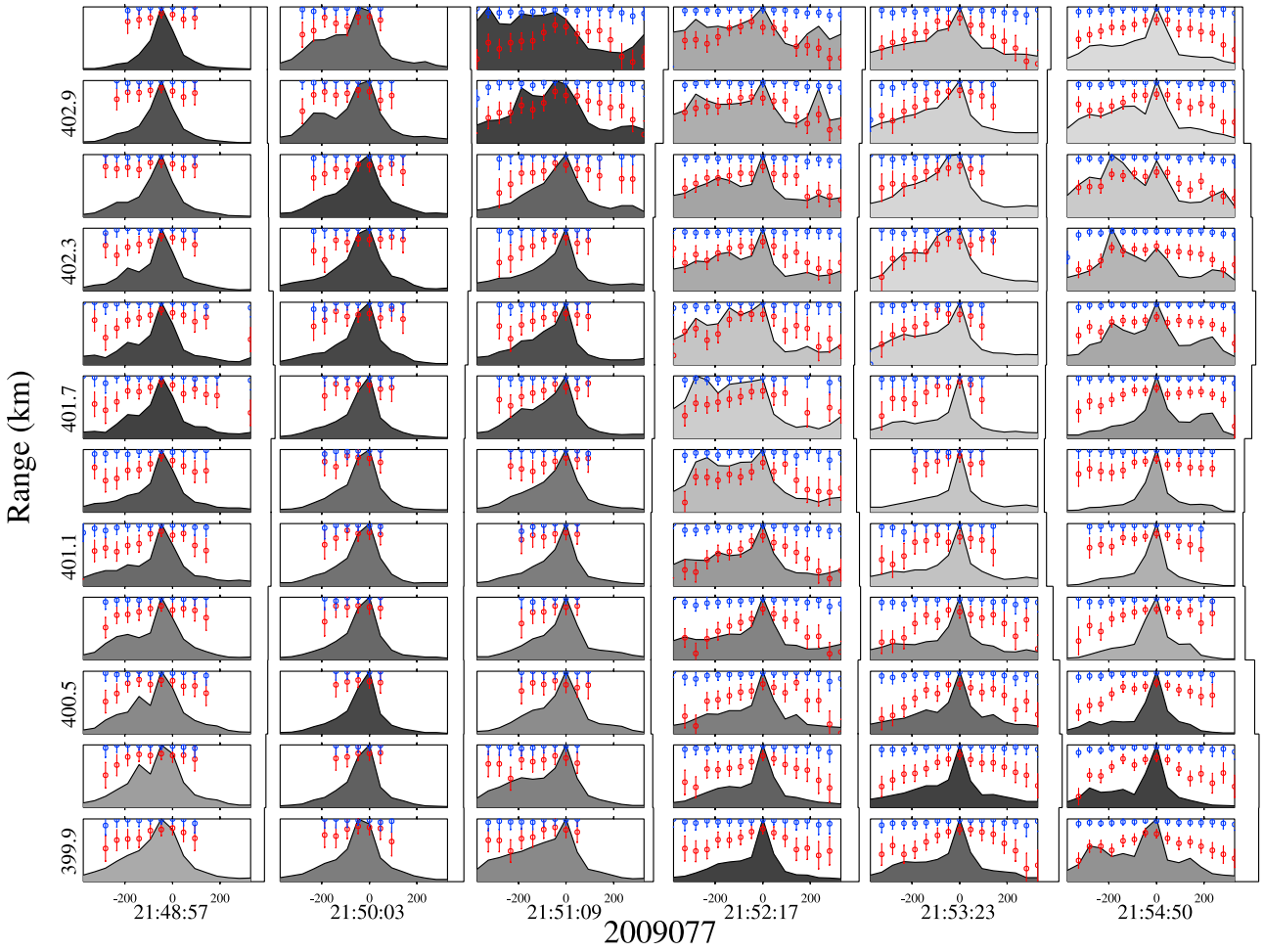

Figure 4. Doppler spectra versus altitude and time. Plotted symbols represent coherence measurements for baseline *ae* (blue) and *cf* (red) on a scale from 0.9–1.0. Symbols are only plotted in spectral bins where the signal-to-noise ratio exceeds 3 dB. Gray scales represent relative peak signal-to-noise ratios on a linear scale within a given column. Bars to the right of the spectra indicate relative average signal-to-noise ratios on a linear scale. Doppler velocities are labeled in m/s. Positive Doppler shifts denote descent, and the tic marks are at ±200 m/s.

waves with wave vectors with different direction cosines and with amplitudes that are statistically independent. Radar interferometry using normalized correlation functions is consequently a super-resolution technique, capable of resolving features beyond the diffraction limit in the high SNR limit.

[26] A more realistic reference model is given by a number of distinct, finite wires randomly distributed in range within a range gate. So long as the wires are parallel, the coherence of the resulting backscatter will remain unity. In fact, the dip angle in the *F* region over Jicamarca varies by about 2×10^{-4} degrees from one end of a 300 m range gate to the other in the *E* and *F* regions. This variation sets the lower limit on the measurable RMS aspect angles of field-aligned irregularities. In practice, systemic and statistical limitations impose considerably larger lower limits than this (see below).

3. Data Presentation

[27] Figure 4 shows Doppler spectra from the ESF event with coherence measurements (on a scale from 0.9–1.0) for two baselines superimposed. Coherence values versus Doppler frequency for baseline *ae* (*cf*) are shown in blue (red), along with error bars calculated using (8). In computing the coherence estimates, the cable length, bias, and baseline alignment corrections described in section 2 were applied.

[28] The spectra are typical for irregularities within radar plumes, exhibiting central peaks with long tails extending toward negative Doppler shifts (upward velocities) and with additional peaks distributed intermittently [e.g., *Woodman and La Hoz*, 1976]. Frequency aliasing is likely taking place, mainly in the positive-going wings of the spectra. Radar imaging studies have shown that multiple peaks typically represent spatial superpositions of irregularities in multiple, depleted plasma channels within the radar illuminated volume [*Hysell*, 2000].

[29] Typical coherence values for the shorter baseline, *ae*, and longer baseline, *cf*, are about 0.995 and 0.975, respectively, although some systematic variations with Doppler frequency are evident in the data. In particular, the coherence tends to be highest at small Doppler shifts and to decrease at both wings of the spectra. The trend is most obvious in data

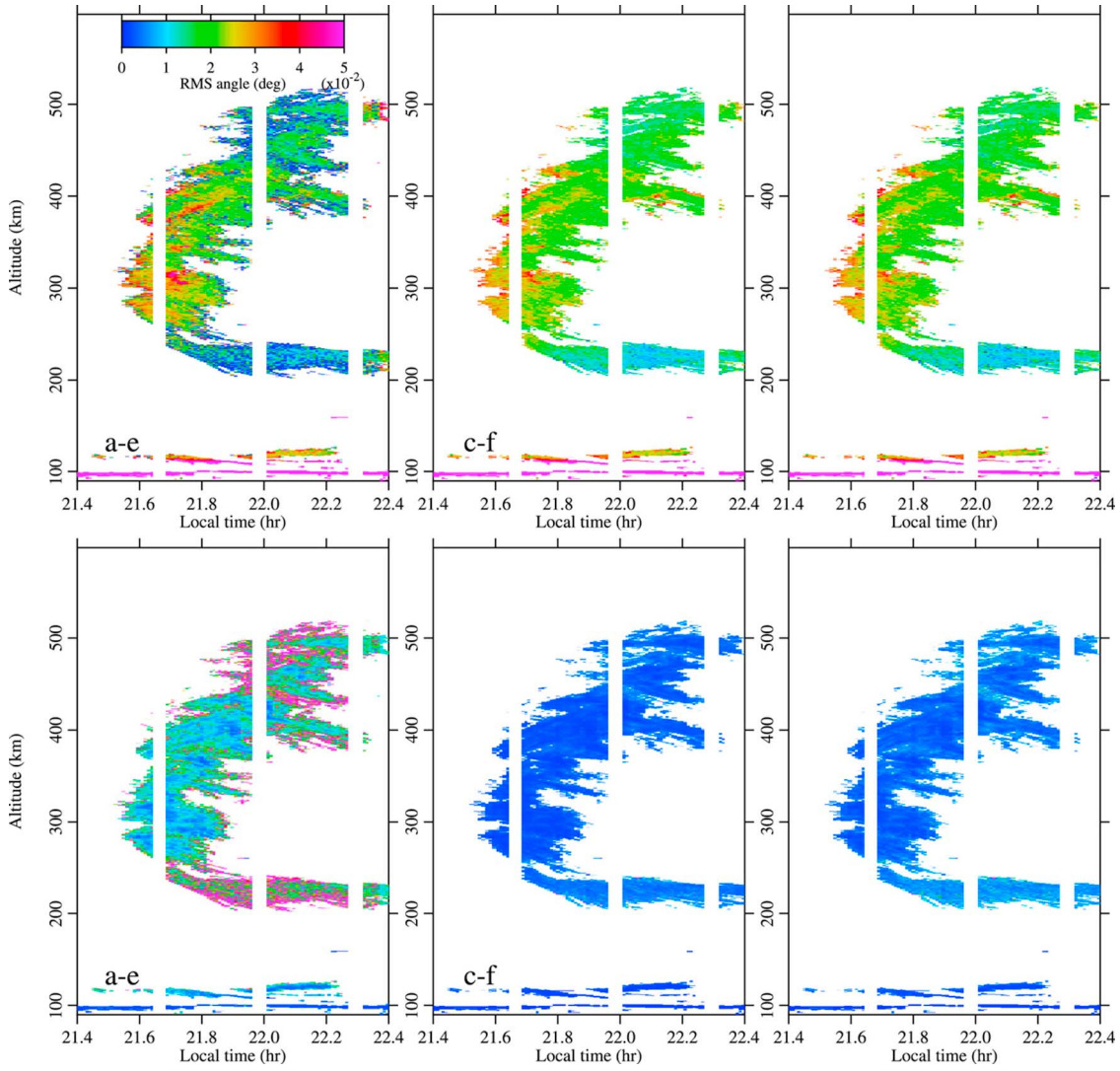

Figure 5. (top) RMS magnetic aspect width of the scatterers estimated using baselines *ae*, and *cf*. (bottom) RMS errors of the magnetic aspect width estimates. The rightmost column represents estimates derived using data from both baselines together (see text). The scales are in *hundredths* of a degree, not degrees.

from the longer baseline but is also mirrored in the shorter baseline data. Previous studies did not display this trend, but the spectra in the 2009 data set are broader than those investigated before. The phenomenon does not appear to be related to problems with noise estimation or other systemic biases or errors.

[30] Although the errors in the coherence of the long-baseline data are larger than those for the short baseline, owing to their coherence being smaller, the long-base data are better conditioned (less sensitive to error growth upon error propagation — see below), and the errors on the magnetic aspect angles derived from them are actually much smaller. We illustrate this by processing and presenting the data somewhat differently.

[31] Figure 5 presents RMS magnetic aspect angle widths (top row) and their errors (bottom row) computed for baselines *ae* and *cf*. It is in this figure that the main results of the paper are to be found. Note that the color scale represents *percent* of a degree here, not degrees. The aforementioned bias and cable length corrections have once again been applied to the calculations, although the baseline misalignment corrections have not. This time, Doppler spectral analysis was performed using only two spectral bins (as opposed to 16 used for Figure 4), and aspect angle data from the low-frequency bin (spanning Doppler velocities between ±187.5 m/s) only was utilized. In this way, information from the central portions of the spectra, where the coherence is generally highest, was extracted.

[32] Figure 5 shows that the RMS errors for the magnetic aspect width are of the order of 0.01° for baseline *ae* but less than about 0.005° for *cf*. The RMS aspect widths themselves derived from baseline *cf* are mainly less than 0.02° in the main ESF plume and about 0.01° or less in the bottomside layer. The aspect angles are moreover somewhat narrower at the top of the plume (at 500 km) than immediately below (between 300–400 km). Broader aspect angles are reported by the figure between about 21.6–21.8 LT in the baseline *cf* panel. Collocated and even more extensive broadening is reported in

the baseline *ae* panel. However, this broadening appears to be an artifact of baseline alignment errors. It is morphologically similar but much more severe still in data for other baselines with even larger misalignments (not shown). That it is more evident in panel *ae* than in panel *cf* is a consequence of the poorer conditioning of the former, i.e., the fact that the transformation from coherence to aspect width is more sensitive to artificial decorrelation the shorter the length of the baseline involved.

[33] That the projections of baselines *ae* and *cf* perpendicular to **B** are very similar (2.74 m and 2.57 m, respectively) suggests that both underlying coherence measurements suffer from nearly the same misalignment error. This coincidence invites a nearly optimal correction strategy. We can solve simultaneous equations (two versions of (5) written for *ae* and *cf*, respectively) for the unknown $\delta\xi_{rms}$, assuming only that $\delta\xi_{rms}$ and $\delta\eta_{rms}$ are the same for both interferometry experiments, or at least that the expansions in (5) hold equally well.

[34] The upper right panel of Figure 5 represents $\delta\xi_{rms}$ found through the aforementioned, combined baseline analysis, and the lower right panel represents the associated statistical errors. The (very minor) correction appears to have removed some of the baseline alignment error from the analysis based on baseline *cf* alone, at the cost of a small increase in the statistical errors. This result represents the best magnetic aspect width measurement possible from the interferometry data available.

[35] The RMS magnetic aspect widths inferred from the combined measurement are found to be very narrow ($\delta\xi_{rms} \lesssim 0.01°$) in the bottomside layer, broader ($\delta\xi_{rms} \sim 0.02°$) in the central portion of the plume, and somewhat narrower again at the top of the plume, approaching $\delta\xi \approx 0.01°$ again. These results are generally consistent with measurements published earlier but are more accurate and comprehensive.

4. Analysis

[36] *Hysell and Farley* [1996] compared the magnetic aspect width measurements available at that time with simple predictions based on the axial ratio of electrostatic irregularities in inhomogeneous, anisotropic, cold fluid plasma in equilibrium as first calculated by *Farley* [1959]. Under that paradigm, the RMS aspect width of the plasma irregularities might be expected to be $\delta\xi_{\rm rms} \approx \sqrt{\nu_i\nu_e/\Omega_i\Omega_e}$, where the ν and Ω factors refer to the collision and gyro frequencies for ions (i) and electrons (e), respectively. Estimates for this factor based on ion-neutral and electron-neutral collision frequencies yield figures of the order of a few hundredths of a degree in the *F* region, in rough agreement with observations. However, the observed aspect widths do not decrease monotonically with altitude the way this formula predicts. Because of this, and because of doubts about the applicability of fluid theory to meter-scale ionospheric phenomena, they rejected this paradigm in favor of one rooted in kinetic theory that included the effects of the background magnetic field, plasma inhomogeneity, and Coulomb collisions.

[37] The *Hysell and Farley* [1996] theory assumes that small-scale plasma irregularities are created through mode coupling to larger-scale irregularities in such a way that the former are initially isotropic. As they decay, they also become more field aligned. The observed aspect width of the irregularities is then their aspect width averaged over their lifetime, weighted by their diminishing intensity. Formally, the mean square aspect angle can be expressed as

$$\langle\theta^2\rangle = \frac{\int_{t_\circ}^{\infty}\int_{-\pi}^{\pi}\theta^2|n_e(\mathbf{k},t)|^2 d\theta dt}{\int_{t_\circ}^{\infty}\int_{-\pi}^{\pi}|n_e(\mathbf{k},t)|^2 d\theta dt} \tag{11}$$

where θ is the magnetic zenith angle of the scattering wave vector **k** which lies in the magnetic meridian plane and satisfies the Bragg scattering condition, $\mathbf{k}(\theta) = (|\mathbf{k}\times\mathbf{B}/B|, \mathbf{k}\cdot\mathbf{B}/B) \sim (|\mathbf{k}|, |\mathbf{k}|\xi)$ defines the decomposition of the scattering wave vector into magnetic perpendicular and parallel components, $|n_e(\mathbf{k}, t)|^2$ is the electron power spectral density at wave vector **k** and time *t*, and where the limits of integration are over all zenith angles and all times after some initial time $t_\circ$. Given an initial condition for the power spectral density and a model for how it dissipates over time, (11) can be used to predict the resulting RMS magnetic aspect angle width (provided that the integrals converge).

[38] *Hysell and Farley* [1996] combined (11) with a two-dimensional kinetic model of small-scale irregularity dissipation and predicted aspect widths that were consistent with observations. Their predictions scaled as $\delta\xi_{\rm rms} \sim \nu_e^{1/2}\nu_{ii}^{1/6}L^{-1/3}$, where ν_{ii} is the ion-ion collision frequency, ν_e includes electron-neutral and electron-ion collisions, and *L* is the transverse plasma density gradient length scale. Overall, the predicted altitude variation was much more gradual than the aforementioned theory of *Farley* [1959] implied, since ν_e here is relatively constant within a few hundred km of the *F* peak, where it has a local maximum.

[39] The dependence of the aspect width on Coulomb collisions may partially explain the apparent broadening seen near *F*-peak altitudes in Figure 5. Another potentially important factor is the *L* parameter, the plasma density gradient scale length associated with the driving background plasma irregularities. Its reciprocal is a measure of how strongly the 3-m irregularities are being pumped locally in physical space. According to the theory, we should expect the aspect widths to be greatest in the central portion of the plume, around the *F* peak and near the main depleted channel, where the steepest density gradients and largest polarization electric fields are normally found. We may also expect aspect width broadening at large Doppler shifts, which represent backscatter from regions of the radar illuminated volume where the flows are most strongly driven. The experimental findings of this paper are therefore broadly consistent with the *Hysell and Farley* [1996] theory, although a quantitative validation has yet to be realized.

5. Conclusions

[40] The 2009 experiments at Jicamarca confirm earlier observations that the RMS magnetic aspect widths of 3-m plasma density irregularities associated with bottomside ESF are of the order of a hundredth of a degree. ($\delta\xi_{rms} \lesssim 0.01 \pm 0.005°$). However, they also suggest some variation with Doppler shift. Furthermore, the aspect widths do not simply decrease monotonically with altitude but appear to broaden in the central core of the ESF plume ($\delta\xi_{rms} \lesssim 0.02 \pm 0.005°$) where the depletions are deepest and the convection is the strongest.

[41] Presently, there is no direct theoretical prediction to test against these observations, although three-dimensional

particle-in-cell simulations of meter-scale irregularities and waves during ESF may eventually produce theoretical insights (M. M. Oppenheim, personal communication, 2011). We have put forward a reference model, whereby large- and intermediate-scale field-aligned irregularities generate small-scale irregularities that are essentially isotropic through nonlinear mode coupling, which acts like scattering in **k** space. The measured RMS aspect width represents a time average over the lifetime of the irregularities, which are diffusively damped. The dominant dissipation mechanism therefore involves transport of scalar variance from field-aligned modes to modes with finite parallel wave numbers. This mechanism is evidently more important than wave steepening, which involves transport from large- to small-scale field-aligned modes.

[42] Our experiment did not address whether the scattering distribution in the magnetic meridian is well approximated by a Gaussian, viz., whether aspect sensitivity measurements conducted with different meridional baselines should yield different estimates for $\delta\xi_{\mathrm{rms}}$ in the absence of statistical errors and biases. Differences between aspect widths measured with baselines *ae* and *cf* in the present experiments fell within experimental error. However, evidence of substantial skewness or kurtosis in the meridional scattering distribution would argue against the reference model and constitute an important new clue regarding small-scale field-aligned irregularity generation. If field-aligned currents are important in ESF, as implied by the measurements of *Stolle et al.* [2006] and the simulations of *Aveiro and Hysell* [2010], the higher moments might reflect this. Future experiments employing even longer meridional antenna baselines might resolve the issue.

[43] In future experiments, it may also be possible to merge the aspect angle experiment with the aperture synthesis imaging experiment at Jicamarca [see *Hysell and Chau*, 2006] and to verify that spatiotemporal regions of weakly and strongly driven flows exhibit smaller and larger magnetic aspect widths as a whole and consistently. Such a finding might help explain why echoes from the wings of the Doppler spectra seem to have large aspect widths. The experiment would necessitate sampling a number of baselines strategically distributed in the plane of the ground. Long meridional interferometry baselines with small alignment errors would simplify the analysis.

[44] **Acknowledgments.** The Jicamarca Radio Observatory is a facility of the Instituto Geofisíco del Perú operated with support from NSF award AGS-0905448 through Cornell University. We appreciate the help of the Jicamarca staff, particularly the operations group.

[45] Robert Lysak thanks the reviewers for their assistance in evaluating this paper.

References

Aveiro, H. C., and D. L. Hysell (2010), Three-dimensional numerical simulation of equatorial *F*-region plasma irregularities with bottomside shear flow, *J. Geophys. Res.*, *115*, A11321, doi:10.1029/2010JA015602.

Farley, D. T. (1959), A theory of electrostatic fields in a horizontally stratified ionosphere subject to a vertical magnetic field, *J. Geophys. Res.*, *64*, 1225–1233.

Farley, D. T. (1969), Incoherent scatter correlation function measurements, *Radio Sci.*, *4*, 935–953.

Farley, D. T., and D. L. Hysell (1996), Radar measurements of very small aspect angles in the equatorial ionosphere, *J. Geophys. Res.*, *101*, 5177–5184.

Farley, D. T., H. M. Ierkic, and B. G. Fejer (1981), Radar interferometry: A new technique for studying plasma turbulence in the ionosphere, *J. Geophys. Res.*, *86*, 1467–1472.

Hildebrand, P. H., and R. S. Sekhon (1974), Objective determination of the noise level in Doppler spectra, *J. Appl. Meteorol.*, *13*, 808–811.

Huba, J. D., and S. L. Ossakow (1979), On the generation of 3-m irregularities during equatorial spread *F* by low-frequency drift waves, *J. Geophys. Res.*, *84*, 6697–6700.

Huba, J. D., and S. L. Ossakow (1981a), On 11-cm irregularities during equatorial spread *F*, *J. Geophys. Res.*, *86*, 829–832.

Huba, J. D., and S. L. Ossakow (1981b), Physical mechanism of the lower-hybrid-drift instability in a collisional plasma, *J. Atmos. Terr. Phys.*, *43*, 775–778.

Hysell, D. L. (2000), A review and synthesis of plasma irregularities in equatorial spread *F*, *J. Atmos. Sol. Terr. Phys.*, *62*, 1037–1056.

Hysell, D. L., and J. L. Chau (2006), Optimal aperture synthesis radar imaging, *Radio Sci.*, *41*, RS2003, doi:10.1029/2005RS003383.

Hysell, D. L., and D. T. Farley (1996), Implications of the small aspect angles of equatorial spread *F*, *J. Geophys. Res.*, *101*, 5165–5176.

Hysell, D. L., J. Chun, and J. L. Chau (2004), Bottom-type scattering layers and equatorial spread *F*, *Ann. Geophys.*, *22*, 4061–4069.

Kudeki, E., and D. T. Farley (1989), Aspect sensitivity of equatorial electrojet irregularities and theoretical implications, *J. Geophys. Res.*, *94*, 426–434.

Leadabrand, R. L., J. C. Schlobohm, and M. J. Baron (1965), Simultaneous, very high frequency and ultra high frequency observations of the aurora at Fraserburgh, Scottland, *J. Geophys. Res.*, *70*, 4235–4284.

Lu, F., D. T. Farley, and W. E. Swartz (2008), Spread in aspect angles of equatorial *E* region irregularities, *J. Geophys. Res.*, *113*, A11309, doi:10.1029/2008JA013018.

Ochs, G. R. (1965), The large 50 Mc/s array at Jicamarca radar observatory, *Tech. Rep. 8772*, U.S. Dep. of Commer., Natl. Bur. of Stand., Gaithersburg, Md.

Oksman, J., M. V. Uspensky, G. V. Starkov, G. S. Stepanov, and M. Villinkoski (1986), The mean fractional electron density fluctuation amplitude derived from auroral backscatter data, *J. Atmos. Terr. Phys.*, *48*, 107–114.

Stolle, C., H. Lühr, M. Rother, and G. Balasis (2006), Magnetic signatures of equatorial spread *F* as observed by the CHAMP satellite, *J. Geophys. Res.*, *111*, A02304, doi:10.1029/2005JA011184.

Thompson, A. R. (1986), *Interferometry and Synthesis in Radio Astronomy*, John Wiley, New York.

Woodman, R. F. (1997), Coherent radar imaging: Signal processing and statistical properties, *Radio Sci.*, *32*, 2373–2391.

Woodman, R. F. (2009), Spread F—An old equatorial aeronomy problem finally resolved?, *Ann. Geophys.*, *27*, 1915–1934.

Woodman, R. F., and C. La Hoz (1976), Radar observations of *F* region equatorial irregularities, *J. Geophys. Res.*, *81*, 5447–5466.

J. L. Chau and M. A. Milla, Radio Observatorio de Jicamarca, Instituto Geofísico del Perú, Lima 33, Peru.

D. T. Farley, R. B. Hedden, and W. E. Swartz, Electrical and Computer Engineering, Cornell University, Ithaca, NY 14853, USA.

D. L. Hysell, Earth and Atmospheric Sciences, Cornell University, Ithaca, NY 14853, USA. (dlh37@cornell.edu)